Atomistic Structure of Transient Switching States in Ferroelectric AlScN

Jiawei Huang,[1,*] Jinyang Li,[2,*] Xinyue Guo,[3,*] Tongqi Wen,[4] David J. Srolovitz,[4,†] Zhen Chen,[5,6,‡] Zuhuang Chen,[2,§] and Shi Liu[7,8,‖]

[1]*Department of Physics, The Hong Kong University of Science and Technology, Clear Water Bay, Hong Kong, China*
[2]*School of Materials Science and Engineering, Harbin Institute of Technology, Shenzhen, Guangdong 518055, China*
[3]*School of Materials Science and Engineering, Tsinghua University, Beijing 100084, China*
[4]*Department of Mechanical Engineering, The University of Hong Kong, Hong Kong, China*
[5]*Beijing National Laboratory for Condensed Matter Physics, Institute of Physics, Chinese Academy of Sciences, Beijing 100190, China*
[6]*School of Physical Sciences, University of Chinese Academy of Sciences, Beijing 100049, China*
[7]*Department of Physics, School of Science, Westlake University, Hangzhou 310030, China*
[8]*Institute of Natural Sciences, Westlake Institute for Advanced Study, Hangzhou 310024, China*

(Received 22 August 2025; accepted 19 December 2025; published 14 January 2026)

We provide atomistic insights into the microscopic mechanism of polarization switching in wurtzite ferroelectric AlScN by integrating advanced thin-film fabrication, ferroelectric switching dynamics characterizations, high-resolution scanning transmission electron microscopy (STEM), and large-scale molecular dynamics simulations enabled by a deep neural network-based interatomic potential. Contrary to earlier interpretations proposing a transient nonpolar intermediate phase, our Letter provides strong evidence that the broad transitional regions previously observed in STEM images are consistent with projection artifacts resulting from the intrinsic three-dimensional zigzag morphology of 180° domain walls, which are a characteristic form of inversion domain boundary. This is further confirmed by STEM imaging of strategically prepared, partially switched $Al_{0.75}Sc_{0.25}N$ thin films. Our simulations reveal that switching proceeds through collective, column-by-column atomic displacements, directly explaining the emergence of zigzag-shaped domain walls, and is consistent with the nucleation-limited switching behavior observed in experimental switching dynamic measurements. Furthermore, we show that increasing Sc content systematically lowers domain wall energy and associated nucleation barrier, thereby reducing the switching field in agreement with experimental trends. These findings establish a direct connection between local domain wall structure, switching dynamics, and macroscopic ferroelectric behavior.

DOI: 10.1103/lfdh-86x6

The discovery of ferroelectricity in wurtzite-structured Sc-doped AlN ($Al_{1-x}Sc_xN$, $0.2 < x < 0.5$) [1] has introduced a promising materials platform for nonvolatile memory technology. The AlN-based ferroelectrics benefit from the industrial maturity of piezoelectric AlN, which has been widely used for decades in applications such as 4G/5G mobile acoustic wave filters [2–5]. Leveraging this established infrastructure, researchers have developed optimized physical vapor deposition processes at sub-400 °C temperatures that are compatible with back-end-of-line semiconductor processing [6,7]. A key breakthrough in enabling ferroelectricity in this system is the incorporation of sufficient Sc dopants into the parent wurtzite AlN lattice, which lowers the energy barrier for polarization switching [1,8]. This compositional tuning transforms $Al_{1-x}Sc_xN$ into a ferroelectric, featuring a wide band gap ($E_g \approx 3$–6 eV) [9], high remanent polarization (P_r) of >70–135 $\mu C/cm^2$ [1], and excellent thermal stability [10,11]. Furthermore, the material exhibits thickness-independent P_r below 10–20 nm scale [12,13], overcoming a major scaling limitation in conventional ferroelectric memory technologies.

Despite these advances, a significant challenge persists: the high coercive fields ($E_c \approx 2$–6 MV/cm) required for polarization reversal approach the dielectric breakdown threshold ($E_{bd} \approx 6$–8 MV/cm), creating a trade-off between switching reliability and dielectric integrity [14–16]. This narrow operating window raises reliability concerns, including high leakage currents and limited endurance. For example, catastrophic leakage currents exceeding 10^3 A/cm^2 have been reported at $x = 0.3$ [17], and endurance failure occurs below 10^5 cycles [18], both orders

*These authors contributed equally to this work.
†Contact author: srol@hku.hk
‡Contact author: zhen.chen@iphy.ac.cn
§Contact author: zuhuang@hit.edu.cn
‖Contact author: liushi@westlake.edu.cn

of magnitude worse than those seen in perovskite and HfO_2-based ferroelectrics [19,20]. Current mitigation efforts include doping and strain engineering [21–24]. Empirically, the coercive field in $Al_{1-x}Sc_xN$ decreases with Sc concentration, following $E_c(x) = -15x + 8.35$ MV/cm for $0 < x < 0.43$ [25]. Additionally, epitaxial tensile strain engineering has been shown to reduce E_c by approximately 30% at 0.8% strain [26].

Nevertheless, these approaches currently lack atomistic design principles due to an unresolved debate over the underlying polarization-switching mechanism. Recent *in situ* scanning transmission electron microscopy (STEM) studies have proposed a transient, low-barrier nonpolar intermediate state, characterized by antipolar arrangements of wurtzite motifs when viewed along the [100] crystallographic direction [27]. However, more recent theoretical and experimental work suggests that switching proceeds through conventional inversion domain boundary (IDB*)-mediated mechanisms in the wurtzite lattice [28–33]. Clarifying this discrepancy is essential for developing reliable atomistic design principles.

By integrating multiscale theoretical modeling with advanced thin-film fabrication and STEM imaging, this Letter provides a comprehensive framework for understanding polarization switching in wurtzite ferroelectrics. Using a deep neural network-based interatomic potential trained on density functional theory (DFT) data, we perform large-scale molecular dynamics (MD) simulations that capture the electric-field-driven 3D evolution of domain structures and transient states in Sc-doped AlN. These simulations reveal that the 180° domain walls exhibit irregular, nonplanar morphology, adopting the conventional IDB* configuration. We suggest that the previously proposed "nonpolar" intermediate state likely arises from projection artifacts caused by the superposition of coexisting metal (M)-polar and nitrogen (N)-polar domains, along with 180° domain walls. The theoretical predictions are supported by the strong agreement between our simulated structural model and high-resolution STEM images of thin films containing both switched and unswitched domains, which were experimentally achieved through tailored electrical pulse engineering. Investigation of the domain wall propagation reveals a stepwise, column-by-column switching pathway. This mechanism provides a natural explanation for the formation of irregular domain morphologies and is consistent with measured switching dynamics. Furthermore, we quantitatively link Sc concentration to reduced domain wall energy and nucleation barrier, providing a microscopic explanation for the doping-dependent decrease in the coercive field.

We begin by characterizing the switching dynamics of fabricated $Al_{0.75}Sc_{0.25}N$ thin films (see details in End Matter). The polarization switching kinetics deviate significantly from classical Kolmogorov-Avrami-Ishibashi (KAI) behavior, instead exhibiting nucleation-limited

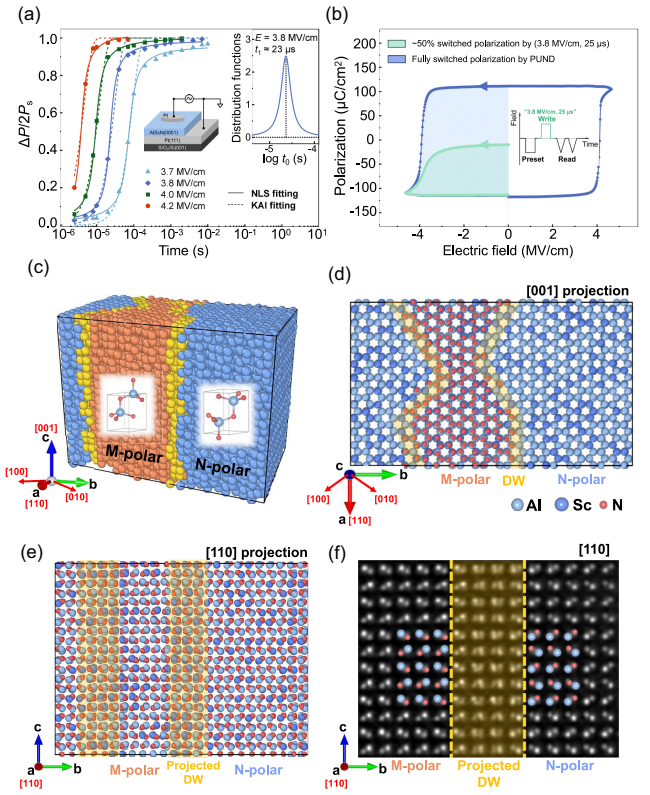

FIG. 1. (a) Switchable polarization measured under various external voltages, fitted using both the KAI and NLS models. The NLS model yields a better fitting. The inset shows the Lorentzian distribution function used in the NLS fitting and a schematic of the Pt/AlScN/Pt capacitor structure. (b) Polarization-electric field hysteresis loops demonstrating the fully switched (100%) and precisely half-switched (50%) polarization states. The inset illustrates the PUND pulse sequence used to achieve the controlled 50% switching. (c) Partially switched $Al_{0.73}Sc_{0.27}N$ supercell obtained with MD simulations. Insets depict local atomic configurations within two oppositely polarized domains, colored in blue and orange. (d) Top view along the [001] direction and (e) front view along the [110] direction of the simulated partially switched structure. (f) High-resolution STEM image showing domain structures in a 50% switched $Al_{0.75}Sc_{0.25}N$ thin film. The transitional region between the dashed yellow lines resembles the yellow-shaded area in panel (e).

switching (NLS) kinetics [Fig. 1(a)]. The extracted distribution of characteristic switching times [Fig. 1(a), inset] provides a quantitative basis for implementing controlled partial switching [34,35]. Leveraging the NLS-derived temporal statistics, we empirically designed an optimized electric-field pulse (3.8 MV/cm, 25 μs) precisely timed to coincide with the peak switching probability, resulting in 50% switched polarization [Fig. 1(b)]. Subsequent polarization mapping confirms that this single-pulse protocol likely produces a state with 50% of the area under the electrode being fully switched and the other half remains unswitched, as STEM imaging only observes M-polar and

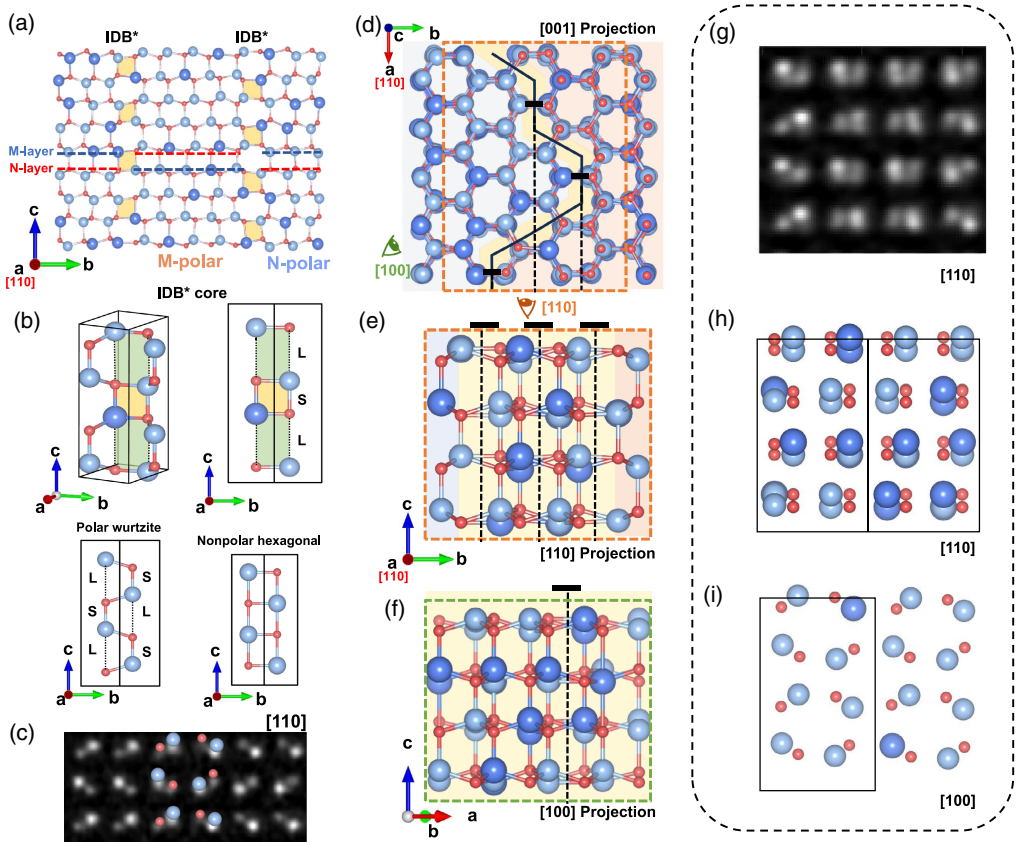

FIG. 2. (a) [110] projection of a two-atomic-layer slice with 180° domain walls. Four-membered bond rings in the IDB* configuration are highlighted in yellow. (b) 3D schematic of an IDB* core, featuring alternating long (L) and short (S) M—N bonds along the c axis. For comparison, the structures of polar wurtzite AlN and the commonly assumed nonpolar hexagonal phase are shown in the lower panel. (c) Experimental STEM image of the IDB* configuration. (d) Top view ([001] projection) of the simulated domain structure. M-polar and N-polar regions are colored blue and red, respectively; domain wall regions are shown in yellow. (e) [110] projection and (f) [100] projection of the structure shown in (d). (g) STEM image adapted from Ref. [27]. An equivalent pattern from our own STEM image is used here. (h) [110] and (i) [100] projections of the proposed nonpolar intermediate phase deduced from (g), reconstructed based on Ref. [27].

N-polar domains. This partially switched sample provides an ideal platform for atomistic structural analysis.

We further use MD simulations to obtain a partially switched state in an $Al_{0.73}Sc_{0.27}N$ supercell of 11 520 atoms (see End Matter). As shown in Fig. 1(c), the supercell contains coexisting N-polar (unswitched) and M-polar (switched) domains. From the top view along the c axis ([001] direction), the interface between oppositely polarized domains forms atomically sharp 180° domain walls [highlighted in yellow in Fig. 1(d)]. This boundary adopts the structure of a conventional IDB* (see discussions below), but unlike the planar wall typical of perovskite ferroelectrics, it exhibits a highly irregular, zigzag morphology. This structural complexity is crucial for interpreting the experimental STEM images. When viewed along the a axis [[110] direction; see front view in Fig. 1(e)], the projected structure appears to exhibit broad transitional regions spanning several atomic layers (highlighted in yellow). Our high-resolution STEM imaging [Fig. 1(f)] of the partially switched $Al_{0.75}Sc_{0.25}N$ sample reveals atomic configurations that closely match the simulated projection [Fig. 1(e)]. The strong agreement suggests that the seemingly broad interfacial regions in the STEM image are consistent with projection effects rather than intrinsic structural features, supporting the existence of irregular, nonplanar 180° domain walls.

To resolve the atomic-scale structure of the 180° domain wall, we analyze a representative two-atomic-layer slice, projected along the [110] direction [Fig. 2(a)]. This configuration exhibits typical features of an IDB*, consistent with Northrup's model [36], including four- and eight-membered bond rings. A three-dimensional view [Fig. 2(b)] reveals that while the four-membered rings are coplanar within the bc plane, the eight-membered rings are buckled, connecting adjacent atomic layers along the a axis. At the core of this IDB*, we observe alternating short (≈1.9 Å) and long (≈3.0 Å) vertical M—N bonds. The observed bond-length alternation signifies a Peierls-like distortion. In contrast, the undistorted paraelectric hexagonal phase, often regarded as the nonpolar reference state for wurtzite ferroelectrics [37–41], features equivalent vertical M—N bonds along the c axis [see Fig. 2(b)]. Importantly,

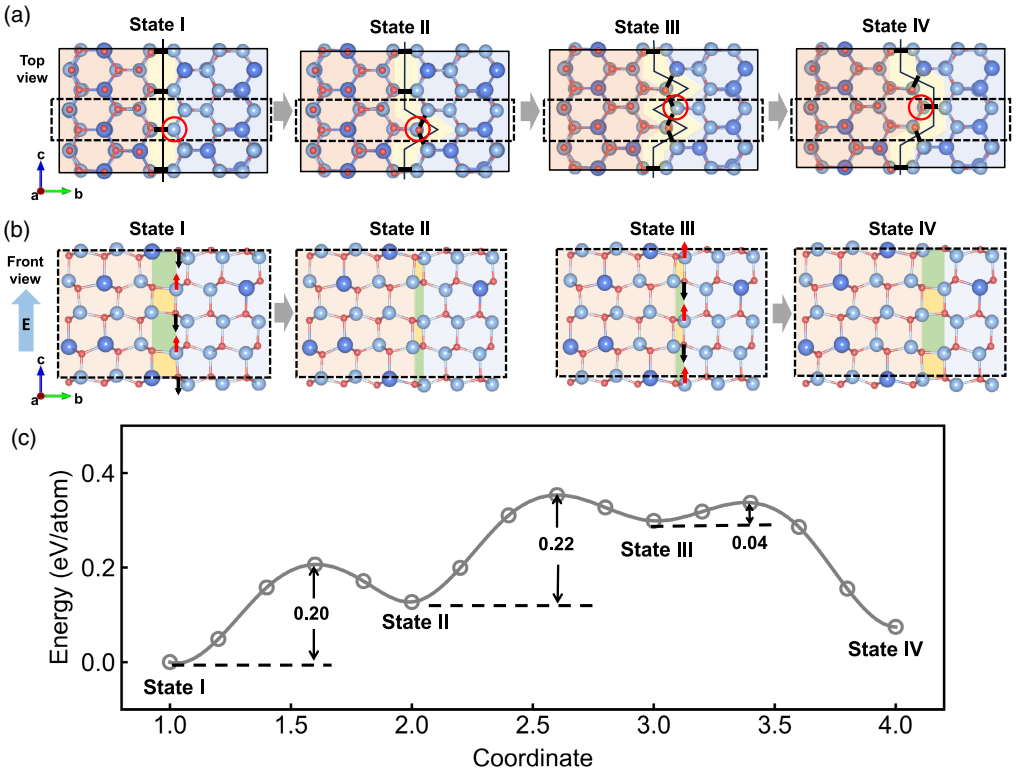

FIG. 3. (a) Key stages of domain wall propagation extracted from MD simulations. Top views show the evolution of the domain wall, starting from a flat interface (state I), progressing through complex intermediate configurations (states II and III), and locally reflattening in state IV. (b) Corresponding front view of a two-atomic-layer slice, highlighted by the dashed rectangle in (a). (c) Energy landscape associated with domain wall propagation process in (a), calculated using the DFT-based CI NEB method.

the characteristic IDB* atomic configuration, including the signature bond rings, is directly resolved in the phase image of a central slice from the multislice electron ptychography (MEP) reconstruction, taken from a region with a locally flat wall aligned with the projection direction in the partially switched film [Fig. 2(c)]. This provides strong experimental evidence for our simulated structural model. Notably, the sharp planar domain wall appears only at a specific depth within a few nanometer thickness range along the projection. Nonplanar 3D nature with superposition of different domain walls still occurs at other depths, as shown in Supplemental Material, Fig. S4 [42].

We now explain how the 3D domain structure with atomically sharp domain walls gives rise to the wide interfacial regions observed in STEM imaging. The simulated top view along the c axis [[001] projection, Fig. 2(d)] shows that the wall meanders laterally across multiple lattice constants along the b axis. Three thick black lines, each orthogonal to a segment of the domain wall aligned with the a axis, indicate the locations of the three IDB* boundaries depicted in Fig. 2(a). When viewed along the a axis [[110] projection, Fig. 2(e)], this zigzag geometry causes overlapping of N-polar and M-polar domains, as well as of the domain wall segments themselves. This results in the appearance of a broad transitional region (yellow-shaded area), an effect that closely matches both our experimental STEM data [Fig. 1(e)] and previous observations [reproduced here as Fig. 2(g)] [27]. The simulated projection along the [100] direction [Fig. 2(f)] again displays features of a transitional region (yellow-shaded area). However, this view differs significantly from that of a previously proposed intermediate state [Fig. 2(i)], which was interpreted as a distinct nonpolar phase with antipolar wurtzite motifs [27]. Our results indicate that such broad transitional features in 2D projections likely arise from projecting a complex 3D domain structure with zigzag, atomically sharp domain walls. We have performed multiple MD simulations across various compositions and electric field strengths, all of which consistently revealed the formation and motion of zigzag-shaped walls (Supplemental Material, Sec. V [42]).

MD simulations show that the switching mechanism in $Al_{0.73}Sc_{0.27}N$ proceeds via localized, collective atomic shifts along the polar axis. As depicted in Fig. 3(a), a typical process begins with an initial flat domain wall (state I). Under an upward electric field, the reversal of a single N-polar column near the wall transforms the local structure into an M-polar configuration, resulting in a more irregular domain boundary (state II). The corresponding front view of a two-atomic-layer slice [dashed rectangle in Fig. 3(a)] shows the field-driven atomic displacements: Al/Sc atoms shift in the direction of the field, while N

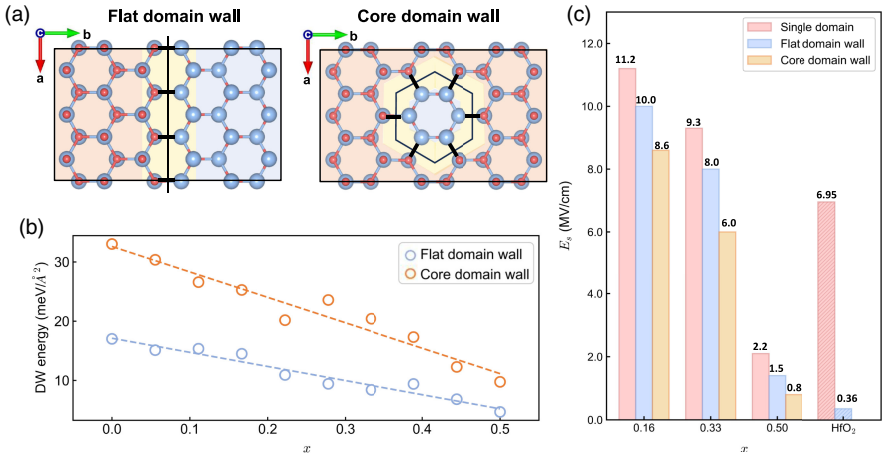

FIG. 4. (a) Schematic of two types of domain walls. (b) Domain wall (DW) energy as a function of Sc concentration (x) for both flat and core domain walls, obtained from MD simulations. (c) Switching field (E_s) as a function of Sc concentration (x) for different domain wall configurations. Reference values of E_s for ferroelectric HfO_2 in single-domain and domain-wall-containing supercells are included for comparison.

atoms move in the opposite direction [see state I to state II in Fig. 3(b)]. The subsequent reversal of adjacent columns further increases the roughness of the domain wall morphology (state III), leading to a rise in interfacial energy. To reduce this energy, the system rapidly evolves into a lower-energy configuration by reestablishing a more locally flat domain boundary (state IV). This relaxation step is again mediated by the reversal of an individual atomic column, as illustrated in the corresponding front view.

The corresponding energy profile for the described process, obtained from DFT-based climbing-image nudged elastic band (CI NEB) calculations, is shown in Fig. 3(c). Unlike previous NEB studies [27,56] which focused on polarization switching in a single-domain supercell, our Letter investigates domain wall motion, as both our large-scale MD simulations and experimental results suggest it is the dominant switching mechanism. We note that the calculated energy barrier per supercell is ≈0.8 eV. In previous studies, the barrier was often normalized by dividing this value by the total number of atoms in the supercell [57–59]. Here, we introduce a normalized energy barrier, defined as the total barrier divided by the number of atoms involved in columnwise switching. The normalized energy barriers for the transitions of state I → state II and state II → state III are each approximately 0.2 eV/atom (Supplemental Material, Sec. IV [42]). Furthermore, the progressive increase in energy from state I to state III indicates that the domain wall energy scales with its roughness. The elevated energy of state III renders it unstable, and the subsequent relaxation to a geometrically simpler configuration (state IV) proceeds via a significantly lower energy barrier of just 0.04 eV/atom. These results offer insight into the microscopic origin of zigzag domain walls. The switching of individual atomic columns at locally flat domain walls involves similar energy barriers, and their spatial separation allows them to act as largely independent switching units. Consequently, switching occurs stochastically, with different columns reversing at different times under the applied electric field. This asynchronous behavior gives rise to rough, nonplanar domain boundaries that manifest as zigzag-shaped walls at larger scales. Moreover, the high energy of irregular configurations like state III drives the system to locally reflatten the wall, reinforcing the dynamic, sawtooth-like morphology of the domain wall.

The established connection between polarization switching and domain wall motion suggests that doping can tune the coercive field by lowering domain wall energy. Since nucleation primarily incurs an energy cost from forming new domain walls [60,61], reducing this energy directly lowers the nucleation barrier. We investigate the effect of Sc concentration on the energetics of two representative domain wall configurations shown in Fig. 4(a): a conventional flat domain wall and a core domain wall, which forms at the interface of a hexagonal, six-atomic-column N-polar nucleus embedded within an M-polar matrix. This quasi-one-dimensional reversed domain, identified in our MD simulations, represents the minimal stable switching unit within a parent domain and may serve as an effective nucleation center. As shown in Fig. 4(b), the formation energies of both types decrease nearly linearly with increasing Sc content. The flat wall energy drops from 17.1 to 4.6 meV/Å^2, while the core domain energy decreases more significantly, from 33.1 to 9.7 meV/Å^2.

We further assess the ease of polarization switching by determining the minimum field strength (E_s) required to induce switching within 100 ps in MD simulations, following a protocol developed in Ref. [62]. This evaluation is performed for single-domain supercells, as well as for systems containing flat and core domain walls. Figure 4(c) reveals several key findings. First, increasing Sc concentration reduces the magnitude of E_s, consistent with experimental observations and attributed to the doping-induced

reduction in domain wall energy. Second, preexisting domain walls further reduce E_s compared to the single-domain case. However, domain-wall-assisted switching is less effective in AlScN. For example, at $x = 0.33$, flat domain walls only moderately reduce the switching field from 9.3 to 8.0 MV/cm. In contrast, ferroelectric HfO_2 exhibits nearly an order-of-magnitude reduction, highlighting the nucleation-limited switching in AlScN. Lastly, core domain walls are more effective than flat ones in lowering the switching field, suggesting a potential design strategy for reducing coercive fields in AlScN systems.

In summary, by integrating multiscale simulations with experimental validation, we present important insights into the polarization switching mechanism in wurtzite ferroelectrics. The broad transitional regions previously observed in STEM images are attributed to projection effects arising from the intrinsic three-dimensional zigzag morphology of 180° domain walls, which are a form of inversion domain boundary. Our analysis reveals that switching proceeds via a highly localized, column-by-column reversal process, consistent with nucleation-limited switching dynamics observed in experiments. The zigzag shape of the domain walls originates from asynchronous switching of individual atomic columns, which roughens the wall morphology under an applied electric field. Moreover, the experimentally observed reduction in coercive field with increasing Sc doping is attributed to a doping-induced decrease in domain wall energy, which lowers the energy barriers for domain nucleation. Together, these findings provide a comprehensive, atomic-scale understanding of ferroelectric switching in AlScN and offer useful guidelines for the design and optimization of wurtzite-based ferroelectric materials.

Acknowledgments—S. L. acknowledges the support from National Natural Science Foundation of China (12574105) and Zhejiang Provincial Natural Science Foundation of China (LR25A040004). The computational resource is provided by the Open Source Supercomputing Center of S-A-I. Z. H. C. acknowledges the financial support from the National Natural Science Foundation of China (52525209, 92477129, and 52372105), Guangdong Basic and Applied Basic Research Foundation (2024B1515120010), and the financial support for outstanding scientific and technological innovation Talents Training Fund in Shenzhen. Z. C. acknowledges the financial support from the National Natural Science Foundation of China (52273227 and U22A6005).

Data availability—The data that support the findings of this article are openly available [63], embargo periods may apply.

[1] S. Fichtner, N. Wolff, F. Lofink, L. Kienle, and B. Wagner, AlScN: A III-V semiconductor based ferroelectric, J. Appl. Phys. **125**, 114103 (2019).

[2] J. Su, F. Niekiel, S. Fichtner, L. Thormaehlen, C. Kirchhof, D. Meyners, E. Quandt, B. Wagner, and F. Lofink, AlScN-based MEMS magnetoelectric sensor, Appl. Phys. Lett. **117**, 132903 (2020).

[3] W. Wang, P. M. Mayrhofer, X. He, M. Gillinger, Z. Ye, X. Wang, A. Bittner, U. Schmid, and J. K. Luo, High performance AlScN thin film based surface acoustic wave devices with large electromechanical coupling coefficient, Appl. Phys. Lett. **105**, 133502 (2014).

[4] C. Fei, X. Liu, B. Zhu, D. Li, X. Yang, Y. Yang, and Q. Zhou, AlN piezoelectric thin films for energy harvesting and acoustic devices, Nano Energy **51**, 146 (2018).

[5] R. M. R. Pinto, V. Gund, R. A. Dias, K. K. Nagaraja, and K. B. Vinayakumar, CMOS-integrated aluminum nitride MEMS: A review, J. Microelectromech. Syst. **31**, 500 (2022).

[6] X. Liu, D. Wang, K.-H. Kim, K. Katti, J. Zheng, P. Musavigharavi, J. Miao, E. A. Stach, R. H. Olsson, and D. Jariwala, Post-CMOS compatible aluminum scandium nitride/2D channel ferroelectric field-effect-transistor memory, Nano Lett. **21**, 3753 (2021).

[7] K. Motoki, Z. Engel, T. M. McCrone, H. Chung, C. M. Matthews, S. Lee, E. N. Marshall, A. Ghosh, A. Tang, and W. A. Doolittle, Improved crystallographic order of ScAlN/GaN heterostructures grown at low temperatures under metal rich surface conditions, J. Appl. Phys. **135**, 135105 (2024).

[8] H. Wang, N. Adamski, S. Mu, and C. G. Van de Walle, Piezoelectric effect and polarization switching in $Al_{1-x}Sc_xN$, J. Appl. Phys. **130**, 104101 (2021).

[9] R. Deng, S. R. Evans, and D. Gall, Bandgap in $Al_{1-x}Sc_xN$, Appl. Phys. Lett. **102**, 112103 (2013).

[10] M. R. Islam, N. Wolff, M. Yassine, G. Schönweger, B. Christian, H. Kohlstedt, O. Ambacher, F. Lofink, L. Kienle, and S. Fichtner, On the exceptional temperature stability of ferroelectric $Al_{1-x}Sc_xN$ thin films, Appl. Phys. Lett. **118**, 232905 (2021).

[11] D. Wang, P. Wang, S. Mondal, S. Mohanty, T. Ma, E. Ahmadi, and Z. Mi, An epitaxial ferroelectric ScAlN/GaN heterostructure memory, Adv. Electron. Mater. **8**, 2200005 (2022).

[12] R. Mizutani, S. Yasuoka, T. Shiraishi, T. Shimizu, M. Uehara, H. Yamada, M. Akiyama, O. Sakata, and H. Funakubo, Thickness scaling of $Al_{0.8}Sc_{0.2}N$ films with remanent polarization beyond 100 $\mu c/cm^{-2}$ around 10 nm in thickness, Appl. Phys. Express **14**, 105501 (2021).

[13] S. Song, D. K. Pradhan, Z. Hu, Y. Zhang, R. N. Keneipp, M. A. Susner, P. Bhattacharya, M. Drndić, R. H. Olsson, and D. Jariwala, Observation of giant remnant polarization in ultrathin AlScN at cryogenic temperatures, arXiv:2503.19491.

[14] S. Fichtner, F. Lofink, B. Wagner, G. Schönweger, T.-N. Kreutzer, A. Petraru, and H. Kohlstedt, Ferroelectricity in AlScN: Switching, imprint and sub-150 nm films, in *2020 Joint Conference of the IEEE International Frequency Control Symposium and International Symposium on Applications of Ferroelectrics (IFCS-ISAF)* (IEEE, Keystone, CO, USA, 2020), pp. 1–4.

[15] J. X. Zheng, D. Wang, P. Musavigharavi, M. M. A. Fiagbenu, D. Jariwala, E. A. Stach, and R. H. Olsson, Electrical breakdown strength enhancement in aluminum scandium nitride through a compositionally modulated

periodic multilayer structure, J. Appl. Phys. **130**, 144101 (2021).
[16] S.-L. Tsai, T. Hoshii, H. Wakabayashi, K. Tsutsui, T.-K. Chung, E. Y. Chang, and K. Kakushima, Field cycling behavior and breakdown mechanism of ferroelectric $Al_{0.78}Sc_{0.22}N$ films, Jpn. J. Appl. Phys. **61**, SJ1005 (2022).
[17] W. Yang, L. Chen, M. Li, F. Liu, X. Liu, C. Liu, and J. Kang, Stress effect on the leakage current distribution of ferroelectric $Al_{0.7}Sc_{0.3}$ N across the wafer, Appl. Phys. Lett. **123**, 132903 (2023).
[18] T. Mikolajick, S. Slesazeck, H. Mulaosmanovic, M. H. Park, S. Fichtner, P. D. Lomenzo, M. Hoffmann, and U. Schroeder, Next generation ferroelectric materials for semiconductor process integration and their applications, J. Appl. Phys. **129**, 100901 (2021).
[19] S. S. Cheema *et al.*, Enhanced ferroelectricity in ultrathin films grown directly on silicon, Nature (London) **580**, 478 (2020).
[20] S. S. Cheema *et al.*, Ultrathin ferroic HfO_2–ZrO_2 superlattice gate stack for advanced transistors, Nature (London) **604**, 65 (2022).
[21] K. R. Talley, S. L. Millican, J. Mangum, S. Siol, C. B. Musgrave, B. Gorman, A. M. Holder, A. Zakutayev, and G. L. Brennecka, Implications of heterostructural alloying for enhanced piezoelectric performance of (Al, Sc)N, Phys. Rev. Mater. **2**, 063802 (2018).
[22] S. Yasuoka, T. Shimizu, A. Tateyama, M. Uehara, H. Yamada, M. Akiyama, Y. Hiranaga, Y. Cho, and H. Funakubo, Effects of deposition conditions on the ferroelectric properties of $Al_{1-x}Sc_xN$ thin films, J. Appl. Phys. **128**, 114103 (2020).
[23] K. Yazawa, D. Drury, A. Zakutayev, and G. L. Brennecka, Reduced coercive field in epitaxial thin film of ferroelectric wurtzite $Al_{0.7}Sc_{0.3}N$, Appl. Phys. Lett. **118**, 162903 (2021).
[24] K. Yazawa, A. Zakutayev, and G. L. Brennecka, A Landau–Devonshire analysis of strain effects on ferroelectric $Al_{1-x}Sc_xN$, Appl. Phys. Lett. **121**, 042902 (2022).
[25] S.-L. Tsai, T. Hoshii, H. Wakabayashi, K. Tsutsui, T.-K. Chung, E. Y. Chang, and K. Kakushima, Room-temperature deposition of a poling-free ferroelectric AlScN film by reactive sputtering, Appl. Phys. Lett. **118**, 082902 (2021).
[26] G. Schönweger, A. Petraru, M. R. Islam, N. Wolff, B. Haas, A. Hammud, C. Koch, L. Kienle, H. Kohlstedt, and S. Fichtner, From fully strained to relaxed: Epitaxial ferroelectric $Al_{1-x}Sc_xN$ for III-N technology, Adv. Funct. Mater. **32**, 2109632 (2022).
[27] S. Calderon, J. Hayden, S. M. Baksa, W. Tzou, S. Trolier-McKinstry, I. Dabo, J.-P. Maria, and E. C. Dickey, Atomic-scale polarization switching in wurtzite ferroelectrics, Science **380**, 1034 (2023).
[28] D. Wang, D. Wang, M. Molla, Y. Liu, S. Yang, S. Yuan, J. Liu, M. Hu, Y. Wu, T. Ma, K. Sun, H. Guo, E. Kioupakis, and Z. Mi, Electric-field-induced domain walls in wurtzite ferroelectrics, Nature (London) **641**, 76 (2025).
[29] N. Wolff, G. Schönweger, I. Streicher, M. R. Islam, N. Braun, P. Straňák, L. Kirste, M. Prescher, A. Lotnyk, H. Kohlstedt *et al.*, Demonstration and stem analysis of ferroelectric switching in MOCVD-grown single crystalline $Al_{0.85}Sc_{0.15}N$, Adv. Phys. Res. **3**, 2300113 (2024).
[30] H. Lu, G. Schönweger, A. Petraru, H. Kohlstedt, S. Fichtner, and A. Gruverman, Domain dynamics and resistive switching in ferroelectric $Al_{1-x}Sc_xN$ thin film capacitors, Adv. Funct. Mater. **34**, 2315169 (2024).
[31] R. Guido, M. Gremmel, T. Mikolajick, S. Fichtner, and U. Schroeder, Ferroelectric $Al_{1-x}Sc_xN$ opposite state retention model based on switching dynamics, Adv. Funct. Mater. **35**, 2421793 (2025).
[32] D. Behrendt, A. Samanta, and A. M. Rappe, Ferroelectric fractals: Switching mechanism of wurtzite AlN, arXiv:2410.18816.
[33] N. Wolff, T. Grieb, G. Schönweger, F. F. Krause, I. Streicher, S. Leone, A. Rosenauer, S. Fichtner, and L. Kienle, Electric field-induced domain structures in ferroelectric AlScN thin films, J. Appl. Phys. **137**, 084101 (2025).
[34] C. Zhou, L. Ma, Y. Feng, C.-Y. Kuo, Y.-C. Ku, C.-E. Liu, X. Cheng, J. Li, Y. Si, H. Huang *et al.*, Enhanced polarization switching characteristics of HfO_2 ultrathin films via acceptor-donor co-doping, Nat. Commun. **15**, 2893 (2024).
[35] R. Guido, H. Lu, P. D. Lomenzo, T. Mikolajick, A. Gruverman, and U. Schroeder, Kinetics of N-to M-polar switching in ferroelectric $Al_{1-x}Sc_xN$ capacitors, Adv. Sci. **11**, 2308797 (2024).
[36] J. E. Northrup and J. Neugebauer, Theory of GaN $(10\bar{1}0)$ and $(11\bar{2}0)$ surfaces, Phys. Rev. B **53**, R10477 (1996).
[37] N. Farrer and L. Bellaiche, Properties of hexagonal ScN versus wurtzite GaN and InN, Phys. Rev. B **66**, 201203(R) (2002).
[38] J. Speck and S. Chichibu, Nonpolar and semipolar group III nitride-based materials, MRS Bull. **34**, 304 (2009).
[39] C. E. Dreyer, A. Janotti, C. G. van de Walle, and D. Vanderbilt, Correct implementation of polarization constants in wurtzite materials and impact on III-nitrides, Phys. Rev. X **6**, 021038 (2016).
[40] J. Huang, Y. Hu, and S. Liu, Origin of ferroelectricity in magnesium-doped zinc oxide, Phys. Rev. B **106**, 144106 (2022).
[41] F. Yang, Physics of ferroelectric wurtzite $Al_{1-x}Sc_xN$ thin films, Adv. Electron. Mater. **11**, 2400279 (2025).
[42] See Supplemental Material at http://link.aps.org/supplemental/10.1103/lfdh-86x6, which includes Refs. [43–55], for sample preparation and characterization, multislice electron ptychography, polarization switching measurement, deep potential, molecular dynamics simulation, composition-driven polar instability in $Al_{1-x}Sc_xN$, and switching energy barrier.
[43] Z. Chen, M. Odstrcil, Y. Jiang, Y. Han, M.-H. Chiu, L.-J. Li, and D. A. Muller, Mixed-state electron ptychography enables sub-angstrom resolution imaging with picometer precision at low dose, Nat. Commun. **11**, 2994 (2020).
[44] Z. Chen, Y. Jiang, Y.-T. Shao, M. E. Holtz, M. Odstrčil, M. Guizar-Sicairos, I. Hanke, S. Ganschow, D. G. Schlom, and D. A. Muller, Electron ptychography achieves atomic-resolution limits set by lattice vibrations, Science **372**, 826 (2021).
[45] Z. Chen, Y. Jiang, D. A. Muller, and M. Odstrcil, Ptychoshelves_em, source code for multislice electron ptychography, Zenodo, 2021, 10.5281/zenodo.4659690.

[46] P. Umari and A. Pasquarello, Ab initio molecular dynamics in a finite homogeneous electric field, Phys. Rev. Lett. **89**, 157602 (2002).
[47] C. H. Skidmore, R. J. Spurling, J. Hayden, S. M. Baksa, D. Behrendt, D. Goodling, J. L. Nordlander, A. Suceava, J. Casamento, B. Akkopru-Akgun *et al.*, Proximity ferroelectricity in wurtzite heterostructures, Nature (London) **637**, 574 (2025).
[48] M. Gremmel and S. Fichtner, The interplay between imprint, wake-up, and domains in ferroelectric $Al_{0.70}Sc_{0.30}N$, J. Appl. Phys. **135** (2024).
[49] A. K. Tagantsev, I. Stolichnov, N. Setter, J. S. Cross, and M. Tsukada, Non-Kolmogorov-Avrami switching kinetics in ferroelectric thin films, Phys. Rev. B **66**, 214109 (2002).
[50] Y. Ishibashi and Y. Takagi, Note on ferroelectric domain switching, J. Phys. Soc. Jpn. **31**, 506 (1971).
[51] J. Y. Jo, H. S. Han, J.-G. Yoon, T. K. Song, S.-H. Kim, and T. W. Noh, Domain switching kinetics in disordered ferroelectric thin films, Phys. Rev. Lett. **99**, 267602 (2007).
[52] K. Okhotnikov, T. Charpentier, and S. Cadars, Supercell program: A combinatorial structure-generation approach for the local-level modeling of atomic substitutions and partial occupancies in crystals, J. Cheminform. **8**, 17 (2016).
[53] X. Wang and D. Vanderbilt, First-principles perturbative computation of dielectric and born charge tensors in finite electric fields, Phys. Rev. B **75**, 115116 (2007).
[54] X. Wang and D. Vanderbilt, First-principles perturbative computation of phonon properties of insulators in finite electric fields, Phys. Rev. B **74**, 054304 (2006).
[55] L. Bellaiche, A. García, and D. Vanderbilt, Electric-field induced polarization paths in $Pb(Zr_{1-x}Ti_x)O_3$ alloys, Phys. Rev. B **64**, 060103(R) (2001).
[56] C.-W. Lee, K. Yazawa, A. Zakutayev, G. L. Brennecka, and P. Gorai, Switching it up: New mechanisms revealed in wurtzite-type ferroelectrics, Sci. Adv. **10**, eadl0848 (2024).
[57] Z. Liu, X. Wang, X. Ma, Y. Yang, and D. Wu, Doping effects on the ferroelectric properties of wurtzite nitrides, Appl. Phys. Lett. **122** (2023).
[58] B. Bhattarai, X. Zhang, W. Xu, Y. Gu, W. Meng, and A. C. Meng, Effect of Sc spatial distribution on the electronic and ferroelectric properties of AlScN, Mater. Horiz. **11**, 5402 (2024).
[59] T. Hwang, W. Aigner, T. Metzger, A. C. Kummel, and K. Cho, First-principles understanding on the formation of inversion domain boundaries of wurtzite AlN, AlScN, and GaN, ACS Appl. Electron. Mater. **6**, 3257 (2024).
[60] S. Liu, I. Grinberg, and A. M. Rappe, Intrinsic ferroelectric switching from first principles, Nature (London) **534**, 360 (2016).
[61] J. Yang, J. Wu, J. Li, C. Zhou, Y. Sun, Z. Chen, and S. Liu, Theoretical lower limit of coercive field in ferroelectric hafnia, Phys. Rev. X **15**, 021042 (2025).
[62] T. Zhu, L. Ma, X. Duan, S. Deng, and S. Liu, Origin of interstitial doping induced coercive field reduction in ferroelectric hafnia, Phys. Rev. Lett. **134**, 056802 (2025).
[63] To support reproducibility and future use, we have deposited the complete raw training dataset and trained model in the Zenodo Public Repository [J. Huang, Supplementary Material: Atomistic structure of transient switching states in ferroelectric AlScN, 2025, 10.5281/ZENODO.17597038].
[64] L. Zhang, J. Han, H. Wang, R. Car, and W. E, Deep potential molecular dynamics: A scalable model with the accuracy of quantum mechanics, Phys. Rev. Lett. **120**, 143001 (2018).
[65] G. Kresse and F. J, Efficient iterative schemes for ab initio total-energy calculations using a plane-wave basis set, Phys. Rev. B **54**, 11169 (1996).
[66] G. Kresse and J. Furthmüller, Efficiency of ab-initio total energy calculations for metals and semiconductors using a plane-wave basis set, Comput. Mater. Sci. **6**, 15 (1996).
[67] J. P. Perdew, K. Burke, and M. Ernzerhof, Generalized gradient approximation made simple, Phys. Rev. Lett. **77**, 3865 (1996).
[68] S. Plimpton, Fast parallel algorithms for short-range molecular dynamics, J. Comput. Phys. **117**, 1 (1995).

End Matter

Experimental method—To experimentally explore the polarization switching process, a 300-nm-thick $Al_{0.75}Sc_{0.25}N$ thin film was deposited on the $SiO_2/Si(001)$ substrate by a custom-built direct current reactive magnetron sputtering. Polarization switching was characterized using a conventional positive-up-negative-down (PUND) pulse sequence on an aixACCT TF3000 analyzer, where switched polarization components ($\pm\Delta P$) were isolated from parasitic currents by differential measurement between switching and nonswitching pulses. All PUND measurements were performed on woken-up capacitors, which require about two initialization cycles to achieve stable and reproducible ferroelectric switching. We find that the as-grown polarization points from the bottom electrode to the top electrode, against the PU measurement polarity (see Supplemental Material, Sec. III [42]). Switching dynamics in $Pt/Al_{0.75}Sc_{0.25}N/Pt$ capacitors were further investigated through a modified PUND sequence with variable-amplitude-duration write pulses and paired read pulses to extract field- and time-dependent switched polarization while correcting for capacitive-leakage contributions. Experiments were conducted using an aberration-corrected JEM-ARM300F2 transmission electron microscope with the cross-sectional specimen extracted from the area below the top electrode on AlScN films. After confirming consistent electrical properties from 15 capacitors across different areas of the film, we selected one representative capacitor for the more resource-intensive microstructural analysis. We applied the MEP method [43–45] to investigate three-dimensional atomic structures with a picometer lateral resolution and nanometer resolution along the depth dimension (Supplemental Material, Secs. I and II [42]).

Computational method—For large-scale MD simulations, we developed a deep neural network-based potential (Deep Potential) [64], trained on 20 000 $Al_{1-x}Sc_xN$ structures with DFT-computed energies and atomic forces (Supplemental Material, Sec. III [42]). The training set covers a broad range of Sc concentrations ($0 \leq x \leq 1$), biaxial strains ($\pm 2\%$), and multiple phases, including wurtzite, hexagonal, zinc blende, and rocksalt. DFT calculations were performed using the Vienna *ab initio* simulation package (VASP) [65,66], with the projector augmented-wave method and the Perdew-Burke-Ernzerhof exchange-correlation functional [67] a plane-wave cutoff of 400 eV, and a k-point spacing of 0.2 $Å^{-1}$. The validated potential is then employed in MD simulations using LAMMPS [68] with a 11 520-atom $Al_{0.73}Sc_{0.27}N$ supercell under NPT conditions at 300 K and 1.013 kPa. An external electric field was applied via the force method [46], which imposes a field-induced force $F_i = Z_i^* \cdot \epsilon$ on each ion i, where Z_i^* is the Born effective charge tensor and ϵ is the electric field. Switching pathways identified in MD were further validated by DFT-based CI NEB calculations, using a force convergence threshold of 0.01 eV/Å.